

Thermal conductivity variation and heat generation effects on magneto-hybrid nanofluid flow in a porous medium with slip condition

Mohamed R. Eid & Mohamed A. Nafe

To cite this article: Mohamed R. Eid & Mohamed A. Nafe (2020): Thermal conductivity variation and heat generation effects on magneto-hybrid nanofluid flow in a porous medium with slip condition, Waves in Random and Complex Media, DOI: [10.1080/17455030.2020.1810365](https://doi.org/10.1080/17455030.2020.1810365)

To link to this article: <https://doi.org/10.1080/17455030.2020.1810365>



Published online: 24 Aug 2020.



Submit your article to this journal [↗](#)



View related articles [↗](#)



View Crossmark data [↗](#)



Thermal conductivity variation and heat generation effects on magneto-hybrid nanofluid flow in a porous medium with slip condition

Mohamed R. Eid ^{a,b} and Mohamed A. Nafe^a

^aDepartment of Mathematics, Faculty of Science, New Valley University, Al-Kharga Egypt; ^bDepartment of Mathematics, Faculty of Science, Northern Border University, Arar, Saudi Arabia

ABSTRACT

The application of hybrid nanoparticles rather than nanoparticles is one of the greatest critical tasks for enhancing heat transfer. Therefore, the purpose of this article is to analyze the flow and heat transfer resulting from an exponentially decreased sheet of hybrid nanoparticles. The magnetite (Fe_3O_4) and copper (Cu) nanoparticle are suspended in ethylene glycol (EG) to form Fe_3O_4 -Cu/EG hybrid nanofluid. The PDEs governing equations of the issue have been solved after conversion to ODEs by using suitable similarity transformations. The resultant system is then solved numerically by the aid of Runge-Kutta-Fehlberg method (RKF45) with the shooting technique. The most important results of this study are the effect of different variable parameters such as permeability of porous media, the stretching/shrinking parameter, heat generation/absorption effect, slip, and nanoparticle volume fraction on the velocity, temperature profiles, skin friction coefficient, and local Nusselt number. Furthermore, the impacts of radiation, magnetohydrodynamic (MHD), suction/injection parameter, and Prandtl number are also taken into consideration. The influence of important physical parameters is discussed through graphs and tables. It is found that the increase of Fe_3O_4 nanoparticle concentration enhances the heat transfer rate of the hybrid nanofluid in a shrinkable case, the opposite happens in a stretchable state.

ARTICLE HISTORY

Received 14 May 2020

Accepted 10 August 2020

KEYWORDS

Hybrid nanofluid; porous medium; MHD; thermal radiation; slip velocity; heat generation/absorption

1. Introduction

Improving heat flow is now a big issue in architecture and manufacturing applications. In certain applications, cooling liquids such as H_2O , $(\text{CH}_2\text{OH})_2$, and hydrothermally conductive oil are utilized to minimize the rise in heat transfer as pure fluids. Nevertheless, in 1995 Choi [1] invented a new category of fluids called nanofluids to enhance heat transfer. He predicted that the inclusion of metal nanoparticle in the base-fluids would increase the thermal conductivity of the regular specific fluid and would increase the operation of these liquids through the heat transfer. Nanofluids are also used for coolants, lubricants, insulation, air conditioning, micro-electronics, processors of computers, etc. Many

researchers analyzed the performance and characteristics of nanofluids experimentally and numerically in various issues. Hwang et al. [2] analyzed the thermal conductivity of various nano-liquids and found that improving nanofluids thermal conductivity was dependent on the volume of the suspended particles, and the nanoparticle and base fluid thermal conductivities. Several researchers also published on the statistical models of nanofluid. Two popular nanofluid models, i.e. the model is suggested by Buongiorno [3] and Tiwari and Das [4], which are considered in the fluid dynamics. Some researchers, including Refs. [5–7] utilized the Buongiorno model of nanofluid [3], in which the results of Brownian diffusion and thermophoresis are taken into consideration. Tiwari and Das [4] model for nanofluids is used in many writers such as Rohni et al. [8]. The latest publication of [9–13] included the detailed analysis of syntheses, stability, thermo-physical characterizations, features, implementations, and potential future guidance of nano-liquids.

A new type of nanofluid called ‘hybrid nanofluids’ is developed to try a different kind of fluid in its place of nanofluid. Hybrid nanofluid consisting of two distinct nanoparticles distributed across the simple fluid. In comparison with simple liquid and nanofluid including single nanoparticles, this type of fluid offers strong thermal properties. Hybrid nanofluids are commonly used in other fields of heat transfer such as electrical refrigeration, reactor conserving, machining coolant, cooling of the nuclear device, transformer cooling, biomedicine, drug reduction, and refrigeration with greater performance relative to nanofluid applicability. For example, Suresh et al. [14] examined the heat transfer of $\text{Al}_2\text{O}_3\text{--Cu}/\text{H}_2\text{O}$ hybrid nanofluid. Baghbanzadeha et al. [15] studied the fabricated of spherical silica/multi-walls carbon nanotube hybrid nanostructures and different nanostructures.

In addition, Nasrin and Alim [16] examined the effect of nanofluids with dual nanoparticle in a flat plate solar collector utilizing the simulation of finite element. The influences of $\text{Al}_2\text{O}_3\text{--Cu}/\text{H}_2\text{O}$ hybrid nanofluid flow and heat transfer properties are expressed by [17] under turbulent conditions. Devi and Devi [18] probed the 3D hybrid $\text{Cu--Al}_2\text{O}_3/\text{H}_2\text{O}$ nanofluid flow problem over an extending surface with applying Newtonian heating. The thermal conductivity of the 0.05–0.6 volume and 25–50°C of $\text{MgO--MWCNTs}/\text{ethylene glycol}$ mixture nanofluid and multiple research methods are estimated by [19]. Later, Devi and Devi [20] researched progress in the heat transfer of nanofluid hybrid $\text{Cu--Al}_2\text{O}_3/\text{water}$ flow over a stretching surface.

Nanofluid heat transfer is highly influenced by various parameters like, base-fluid choice, size of nanoparticles, viscosity of the nanoparticles, temperature of fluid and stability, nanoparticle dispersion, nanoparticle cleanliness, preparation process, nanoparticle size and shape and nanoparticle compatibility leading to the harmonious mixture of the nanofluid. Hady et al. [21–25] examined the flow of boundary-layer and nanofluid heat transfer over different surfaces in a porous material. For different forms of nanoparticle, Refs. [26–35] elucidated a laminar nanofluid flow through multiple surfaces for varied nanoparticle kinds. They studied the unsteady and steady flow, heat transport and nanoparticles concentration. Qayyum et al. [36] checked the impact on the homogeneous, heterogeneous reactions of nonlinear thermal radiation of silver and copper nanoparticles. They found that the surface temperature quickly increases for $\text{Ag}/\text{H}_2\text{O}$ than $\text{Cu}/\text{H}_2\text{O}$ nanofluids. Later, the thermal radiation and melting heat impacts of carbon– H_2O nanofluid stagnation point flow is elaborated by [37]. They detected that with greater melting parameters and a smaller nanoparticle volume percentage, the skin friction coefficient can be decreased. The aqueous $\text{Al}_2\text{O}_3/\text{Ag}$ mixture nanofluid thermal conductivity at various heat and mass

rates are experimentally studied recently by Aparna et al. [38]. Gulzar et al. [39] recently studied experimental steadiness and rheological features of mixture $\text{Al}_2\text{O}_3/\text{TiO}_2$ Therminol-55 nanofluid in solar concentrations. The stretching plate fluid dynamics have significant implementations in manufacturing such as cable designing, hot roll, and fiberglass processing.

In the same direction, Magyari and Keller [40] tend to be the headmost to look at the wall temperature distribution of flux and the heat transfer properties of an exponentially extended surface. They elaborated the thermal boundary-layer thickness is reduced, with a temperature profile being increased for a constant Prandtl number. The temperature gradient of surface upsurges which means that the heat transfer is accelerated on the plate. Hence, this issue is probed by numerous scientists in the presence of different physical factors. El-Aziz [41] considered the effect of Eckert number on a flow of micropolar fluid. He observed that an improvement in the parameter of micropolar allowed the sheet to cool more rapidly for forced convection flow, whilst the impact of viscous dissipation decreased the rate of heat transport. Furthermore, the influence of non-linear radiation is taken into account by [42–45], and the issue is solved by utilizing the homotopy analysis (HAM) and the Keller-box methods, respectively. In the meantime, Bhattacharyya and Pop [46] elaborated this study on the existence of the magnetic field. After that, Refs. [47,48] measured both non-linear radiation and magnetic parameter impacts whilst working, they observed that the influence of the parameters of radiation and magnetic field decreases Nusselt number for a constant value of Prandtl number. More recent computational studies of nanofluids and hybrid nanofluids in different cases include in [11,49].

This new kind of nanofluids has an exceptional replacement potential in medium temperature implementations like solar collectors and heat exchanger framework as advanced heat transfer fluids. The magnetic nano-composites are excellent support for catalysts, and also the fast, economical, and promising magnetic isolation from the reaction mix for industrial applications. Therefore, the aim of the present paper is to investigate the influence of thermal conductivity variation and heat generation on magneto-hybrid nanofluid flow in a porous material with slip velocity through an exponentially stretching/shrinking surface. The suspension of two separate nanoparticles to form a hybrid nanofluid which is Fe_3O_4 and Cu in EG. MHD and non-linear thermal radiation impacts are also included into the problem model. The governing equations with boundary conditions transformed into a system of ODEs by using similarity transformations and their solutions are obtained using Runge–Kutta–Fehlberg (RKF45) technique.

2. Flow problem analysis

We now propose a laminar steady two-dimensional MHD hybrid nanofluid flow through an exponentially stretching/shrinking sheet embedded in a porous medium. As explained in Figure 1, where x - and y - axes are the coordinates directions, the x - axis is along with the sheet and the y -axis is perpendicular to it. The surface velocity is taken as $u_w(x) = U_0 e^{x/L}$ where U_0 is constant and L is the distinguishing length of the surface. The magnetic field $B(x) = B_0 e^{x/2L}$ is executed along the y -axis where B_0 is the fixed magnetic strength. When studying the hybrid nanofluid, the nanoparticle size is believed to remain constant and the effect on the thermo-physical properties of the nanoparticle accumulation is overlooked due to the mixture nanofluid is fabricated as a stable composite.

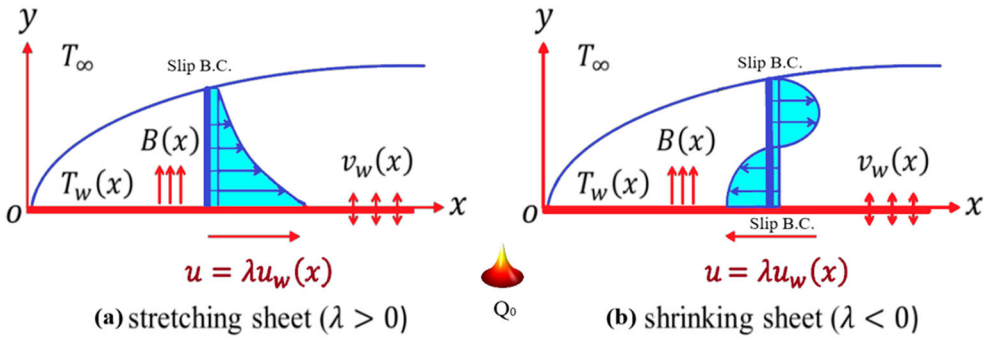


Figure 1. Flow coordinate system.

Therefore, on employing the normal boundary-layer approximation, the hybrid nanofluid leading equations are defined as [50–51]:

$$\frac{\partial u}{\partial x} + \frac{\partial v}{\partial y} = 0 \quad (1)$$

$$u \frac{\partial u}{\partial x} + v \frac{\partial u}{\partial y} = \frac{\mu_{hnf}}{\rho_{hnf}} \frac{\partial^2 u}{\partial y^2} - \frac{\sigma_{hnf}}{\rho_{hnf}} B^2 u - \frac{\mu_{hnf}}{\rho_{hnf}} \frac{\varepsilon}{K_1} u \quad (2)$$

$$u \frac{\partial T}{\partial x} + v \frac{\partial T}{\partial y} = \frac{k_{hnf}}{(\rho c_p)_{hnf}} \frac{\partial^2 T}{\partial y^2} - \frac{1}{(\rho c_p)_{hnf}} \frac{\partial q_r}{\partial y} + \frac{1}{(\rho c_p)_{hnf}} \left\{ \frac{\partial}{\partial y} \left[k_{hnf}^*(T) \frac{\partial T}{\partial y} \right] \right\} + \frac{Q_0}{(\rho c_p)_{hnf}} (T - T_\infty) \quad (3)$$

with the related boundary conditions as follows:

$$\left. \begin{aligned} v = v_w, u = \lambda u_w, T = T_w(x) + D_1 \left(\frac{\partial T}{\partial y} \right) \text{ at } y = 0, \\ u \rightarrow 0, T \rightarrow T_\infty \text{ as } y \rightarrow \infty, \end{aligned} \right\} \quad (4)$$

where u and v symbols to the velocity of a hybrid nanofluid along the x - and y -axes. v_w is the suction/injection parameter, T indicates to the temperature, T_w is the wall temperature, T_∞ symbols to the fixed ambient temperature, and T_0 sings to surface temperature. While q_r is the thermal radiation, ε is the porosity, D_1 represents to the slip parameter, Q_0 is the heat generation/absorption, K_1 is the permeability, and λ is the stretching or shrinking parameter. Observed that, the surface is extended when $\lambda > 0$, dwindled when $\lambda < 0$, and static when $\lambda = 0$.

Taking the approximation of Rosseland for radiation, the radiative heat flux q_r is defined as [52]:

$$q_r = -\frac{4\sigma^*}{3k^*} \frac{\partial T^4}{\partial y} \quad (5)$$

where σ^* is the constant of Stefan–Boltzmann and k^* is the coefficient of mean absorption. Supposing the temperature variance within the flow is such that T^4 can be extended in a Taylor series about T_∞ and ignoring higher-order relations. This result is the following approximation: $T^4 \cong 4T_\infty^3 T - 3T_\infty^4$. Then $\frac{\partial q_r}{\partial y} = -\frac{16\sigma^* T_\infty^3}{3k^*} \frac{\partial^2 T}{\partial y^2}$ and hence the energy

Equation (3) takes the form:

$$u \frac{\partial T}{\partial x} + v \frac{\partial T}{\partial y} = \left[\frac{k_{hnf}}{(\rho c_p)_{hnf}} + \frac{1}{(\rho c_p)_{hnf}} \frac{16\sigma^* T_\infty^3}{3k^*} \right] \frac{\partial^2 T}{\partial y^2} + \frac{1}{(\rho c_p)_{hnf}} \left\{ \frac{\partial}{\partial y} \left[k_{hnf}^*(T) \frac{\partial T}{\partial y} \right] \right\} + \frac{Q_0}{(\rho c_p)_{hnf}} (T - T_\infty) \quad (6)$$

where ρ_{hnf} symbols to density, μ_{hnf} signs to dynamic viscosity, k_{hnf} is hybrid nanofluid thermal conductivity, σ_{hnf} is the electrical conductivity, and $(\rho c_p)_{hnf}$ indicates to heat capacitance of the hybrid nanofluid, respectively. In the meantime, the sub-indexes hnf , nf , f , n_1 , and n_2 are utilized to indicate the hybrid nanoliquid, nanoliquid, EG, Fe_3O_4 and Cu nanoparticle combinations, respectively. As suggested by Dinarvand [51], we use the equations to test the nanofluid and hybrid nanofluid thermo-physical properties as given in Table 1. Moreover, the values of physical features of the investigated base fluid ethylene glycol (EG), magnetite (Fe_3O_4) and Cu are written in Table 2. By using similarity transformations as next [50]:

$$\left. \begin{aligned} u &= U_0 e^{x/L} f'(\eta), v = -\sqrt{\frac{U_0 \nu_f}{2L}} e^{x/2L} [f(\eta) + \eta f'(\eta)], \\ \psi &= \sqrt{2U_0 \nu_f L} f(\eta) e^{x/2L}, \theta(\eta) = \frac{T - T_\infty}{T_w - T_\infty}, \eta = y \sqrt{\frac{U_0}{2\nu_f L}} e^{x/2L} \end{aligned} \right\} \quad (7)$$

where ψ is the stream function which definite as $u = \partial \psi / \partial x$ and $v = \partial \psi / \partial y$. Utilizing these determinations, the equation of continuity (1) is completely contented, so that:

$$f_w = -v_w \sqrt{\frac{2L}{\nu_f U_w}} \quad (8)$$

here $f(0) = f_w$ is the suction or injection parameter (with $f_w < 0$ for injection and $f_w > 0$ for suction), $k_{hnf}^*(T) = k_{hnf} \left(1 + \epsilon \frac{T - T_\infty}{T_w - T_\infty} \right)$ (variable thermal conductivity). Thus, Equations (2) and (3) become:

$$\frac{\mu_{hnf}/\mu_f}{\rho_{hnf}/\rho_f} f'''' + f f'' - 2f'^2 - \left(\frac{\sigma_{hnf}/\sigma_f}{\rho_{hnf}/\rho_f} M - \frac{\mu_{hnf}/\mu_f}{\rho_{hnf}/\rho_f} K \right) f' = 0 \quad (9)$$

$$\left[\frac{k_{hnf}}{k_f} (2 + \epsilon \theta) + \frac{4}{3} R \right] \theta'' + Pr[(\rho c_p)_{hnf}/(\rho c_p)_f] (f \theta' - f' \theta) + \epsilon (k_{hnf}/k_f) \theta'^2 + Prs \theta = 0 \quad (10)$$

Table 1. Nanofluid and hybrid nanofluid thermo-physical characteristics.

Characteristic	Single nanoparticle case	Hybrid nanoparticles case
ρ	$\rho_{nf} = (1 - \varphi_1) \rho_f + \varphi_1 \rho_{n_1}$	$\rho_{hnf} = (1 - \varphi_2)[(1 - \varphi_1) \rho_f] + \varphi_2 \rho_{n_2}$
ρc_p	$(\rho c_p)_{nf} = (1 - \varphi_1)(\rho c_p)_f + \varphi_1 (\rho c_p)_{n_1}$	$(\rho c_p)_{hnf} = (1 - \varphi_2)[(1 - \varphi_1)(\rho c_p)_f + \varphi_1 (\rho c_p)_{n_1}] + \varphi_2 (\rho c_p)_{n_2}$
μ	$\mu_{nf} = \frac{\mu_f}{(1 - \varphi_1)^{2.5}}$	$\mu_{hnf} = \frac{\mu_f}{(1 - \varphi_1)^{2.5} (1 - \varphi_2)^{2.5}}$
k	$k_{nf} = \frac{k_{n_1} + 2k_f - 2\varphi_1(k_f - k_{n_1})}{k_{n_1} + 2k_f + \varphi_1(k_f - k_{n_1})} \times k_f$	$k_{hnf} = \frac{k_{n_2} + 2k_{nf} - 2\varphi_2(k_{nf} - k_{n_2})}{k_{n_2} + 2k_{nf} + \varphi_2(k_{nf} - k_{n_2})} \times k_{nf}$
σ	$\sigma_{nf} = 1 + \frac{3\left(\frac{\sigma_{n_1}}{\sigma_f} - 1\right)\varphi_1}{2 + \frac{\sigma_{n_1}}{\sigma_f} - \left(\frac{\sigma_{n_1}}{\sigma_f} - 1\right)\varphi_1} \times \sigma_f$	$\sigma_{hnf} = \frac{\sigma_{n_2} + 2\sigma_{nf} - 2\varphi_2(\sigma_{nf} - \sigma_{n_2})}{\sigma_{n_2} + 2\sigma_{nf} + \varphi_2(\sigma_{nf} - \sigma_{n_2})} \times \sigma_{nf}$

Table 2. Thermal characteristics of ethylene glycol (EG), magnetite (Fe₃O₄) and copper (Cu).

Characteristic	EG	Fe ₃ O ₄	Cu
c_p (Jkg ⁻¹ K ⁻¹)	2430	2090	385
ρ (kgm ⁻³)	1115	5180	8933
k (Wm ⁻¹ K ⁻¹)	0.253	0.15	400
σ (S/m)	1.07×10^{-1}	2500	5.96×10^7

subject to:

$$\left. \begin{aligned} f(0) = f_w, f'(0) = \lambda, \theta(0) = 1 + \delta\theta'(0), \\ f'(\infty) \rightarrow 0, \theta(\infty) \rightarrow 0. \end{aligned} \right\} \quad (11)$$

here the marking (') indicates to the derivative with respect to η , where $R = \frac{4\sigma^* T_\infty^3}{k^* k}$ represent the radiation parameter, $Pr = \frac{\mu_f(C_p)_f}{k_f}$ represents the Prandtl number, $v_f = \frac{\mu_f}{\rho_f}$, $u_w = U_0 e^{x/L}$, $B = B_0 e^{x/2L}$, $M = \frac{2LB_0^2}{U_0} \frac{\sigma_f}{\rho_f}$ represent the magnetic parameter, $K = \frac{\epsilon}{K_1} \frac{2v_f L}{u_w}$, $s = \frac{2L}{u_w} \frac{Q_0}{(\rho c_p)_f}$ (heat generation/absorption), $\delta = D_1 \sqrt{\frac{u_w}{2v_f L}}$ (slip parameter), and ϵ is a thermal conductivity variation parameter. The skin friction coefficient C_f and the Nusselt number Nu_x are specified as:

$$C_f = \frac{\tau_w}{\rho_f u_w^2}, Nu_x = \frac{2Lq_w}{k_f(T_w - T_\infty)} \quad (12)$$

where the wall shear stress τ_w and the wall heat flux q_w are defined by:

$$\tau_w = \mu_{hnf} \left(\frac{\partial u}{\partial y} \right)_{y=0}, q_w = -k_{hnf} \left(\frac{\partial T}{\partial y} \right)_{y=0} + (q_r)_{y=0} \quad (13)$$

Using Equations (7), (12) and (13) we obtain:

$$Re_x^{1/2} C_f = \frac{\mu_{hnf}}{\mu_f} f''(0), Re_x^{-1/2} Nu_x = - \left(\frac{k_{hnf}}{k_f} + \frac{4}{3} R \right) \theta'(0) \quad (14)$$

where $Re_x = \frac{2Lu_w}{v_f}$ is the Reynolds number.

3. Numerical procedure

The resulting Equations (9–11) are quite non-linear and its solutions in closed form are also not in fact feasible. This issue can be overcome numerically by using RK45 method with the shooting technique with different parameter values. The step size is taken $\Delta\eta = 0.01$ and precision is up to the 5th decimal point as the principle of convergence. We supposed an appropriate finite value for the far-field boundary-condition in (11), i.e. $\eta \rightarrow \infty$, say η_∞ .

$$f'(\eta_\infty) = \theta(\eta_\infty) \rightarrow 0 \quad (15)$$

In all graphs, we established the subsequent parameter values unless otherwise declared.

$$\begin{aligned} M = 0.5, K = 5, \epsilon = 0.2, R = 0.2, Pr = 6.2, s = 0.1, f_w = 0.1, \lambda = 1, \delta = 0.5, \\ \varphi_1 = 0.02, \varphi_2 = 0.04. \end{aligned} \quad (16)$$

4. Results and discussion

With the aid of RKF45 depending on the shooting technique, Equations (9–11) are resolved numerically. Also, the suitable boundary layer thickness, η_∞ needs to be chosen according to the amounts of the specified variables. Here, we have reserved a finite value of η_∞ in the series of $5 \leq \eta_\infty \leq 40$. The values of the local Nusselt number $-\theta'(0)$ for normal fluid ($\varphi_1 = \varphi_2 = 0$) when $f_w = 0$ and $\lambda = 1$ (stretching surface) under various values of Pr , M and R are offered in Table 3. Table 3 displays the contrast with the current literature findings in the particular case of the present analysis of the actual numerical results obtained by RKF45. The present findings display outstanding consistency with those obtained from the preceding literature as seen in Table 3. The numerical outcomes provided in these tables can also be used to compare the other numerical results from various methods, i.e. the shooting methods, bvp4c, and the Keller-box. Depend on this comparison, we establish that RKF45 provided positive solutions comparable to the numerical methods listed above. The consequences of the velocity distribution, temperature distribution, the drag force, and heat transfer rate distribution for various amounts of the controlling parameters are presented in graphs (2–27). Figures 2–21 display the dimensionless velocity profile $f'(\eta)$ and the dimensionless temperature profile $\theta(\eta)$ for different values of permeability of porous media parameter K , parameter ϵ , heat generation/absorption parameter s , the solid volume fraction of Fe_3O_4 parameter φ_1 , and solid volume fraction of Cu parameter φ_2 in stretching ($\lambda > 0$) and shrinking ($\lambda < 0$) cases.

Figures 2 and 3 present the impact of permeability of porous media parameter K on velocity profile for hybrid nanofluids, for fixed amounts of other parameters. It is observed that growing values of permeability of porous media parameter K reduce the velocity and as a consequence, the velocity boundary layer thickness is decreased in the case of stretching ($\lambda > 0$) as demonstrated in Figure 2. This is result in the permeability raises, it declines the magnitude of the force of Darcian body and decelerates the fluid velocity in the boundary-layer, where the velocity and the momentum boundary-layer thickness get larger in the situation of shrinking ($\lambda < 0$), as displayed in Figure 3. Figures 4 and 5 depict the effects of permeability of porous media parameter K on temperature profile $\theta(\eta)$ for ($\lambda > 0$) and ($\lambda < 0$), respectively. It is shown that temperature profile is increased by promoting the permeability parameter K and the thermal boundary-layer thickness also is raised in the case of ($\lambda > 0$) as shown in Figure 4. But it is decreased in the case of ($\lambda < 0$) as seen in Figure 5. From Figures 6 and 7 it is observed that the increasing values of parameter ϵ reduces the

Table 3. $-\theta'(0)$ values for diverse values of Pr , M and R via stretching sheet ($\lambda = 1$) and base fluid ($\varphi_1 = \varphi_2 = 0$) when $f_w = 0$.

Pr	M	R	Ref. [40]	Ref. [41]	Ref. [43]	Ref. [48]	Ref. [50]	Present work
0.5	0	0	0.594338	0.594493	–	–	0.594339	0.594366
1	0	0	0.954782	0.954785	0.9548	0.9548	0.954783	0.954801
2	0	0	–	–	1.4714	1.4715	1.471460	1.471482
3	0	0	1.869075	1.869074	1.8691	1.8691	1.869074	1.869075
5	0	0	2.500135	2.500132	–	2.5001	2.500132	2.500133
10	0	0	3.660379	3.660372	–	3.6604	3.660372	3.660381
1	1	0	–	–	–	0.8611	0.861094	0.861095
1	0	1	–	–	0.5315	0.5312	0.531158	0.531157
1	1	1	–	–	–	0.4505	0.450536	0.450538

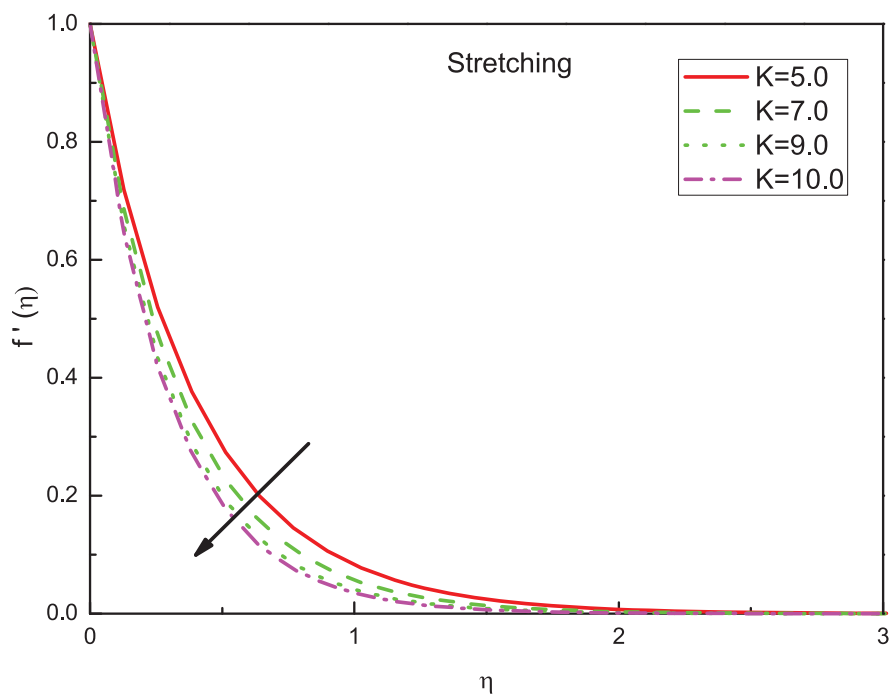


Figure 2. Variation of $f'(\eta)$ vs. K in stretching case.

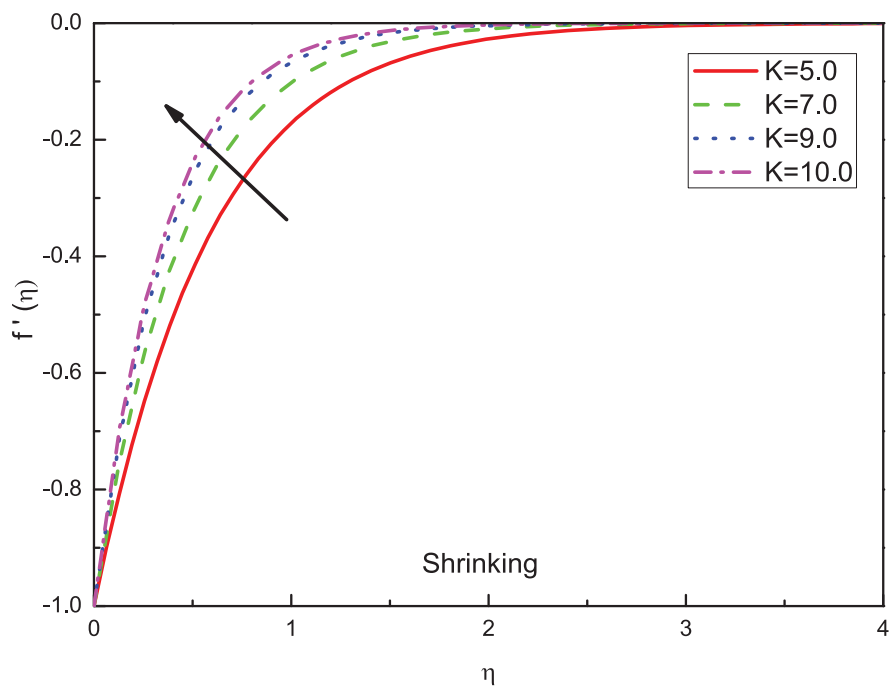


Figure 3. Variation of $f'(\eta)$ vs. K in shrinking case.

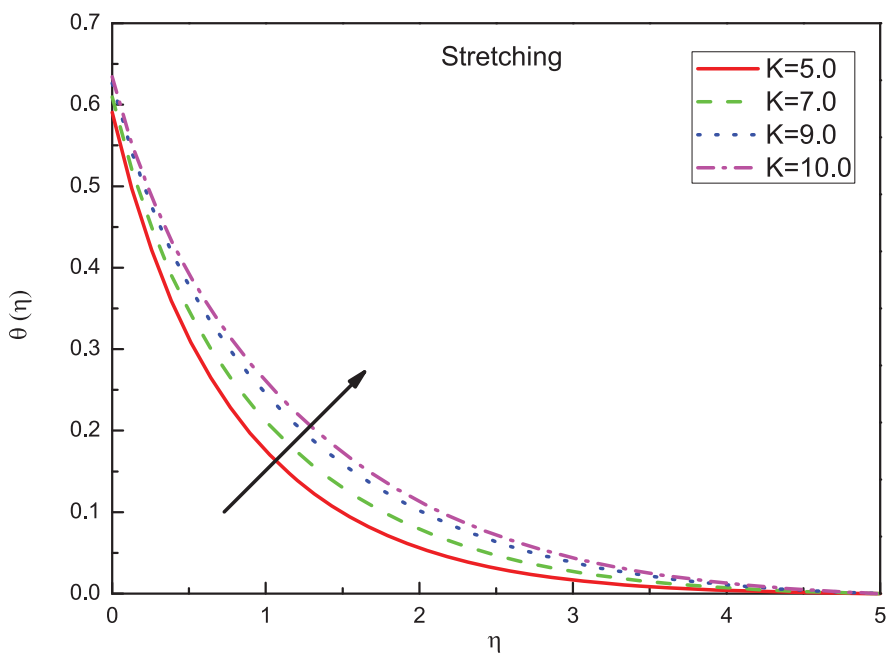


Figure 4. Variation of $\theta(\eta)$ vs. K in stretching case.

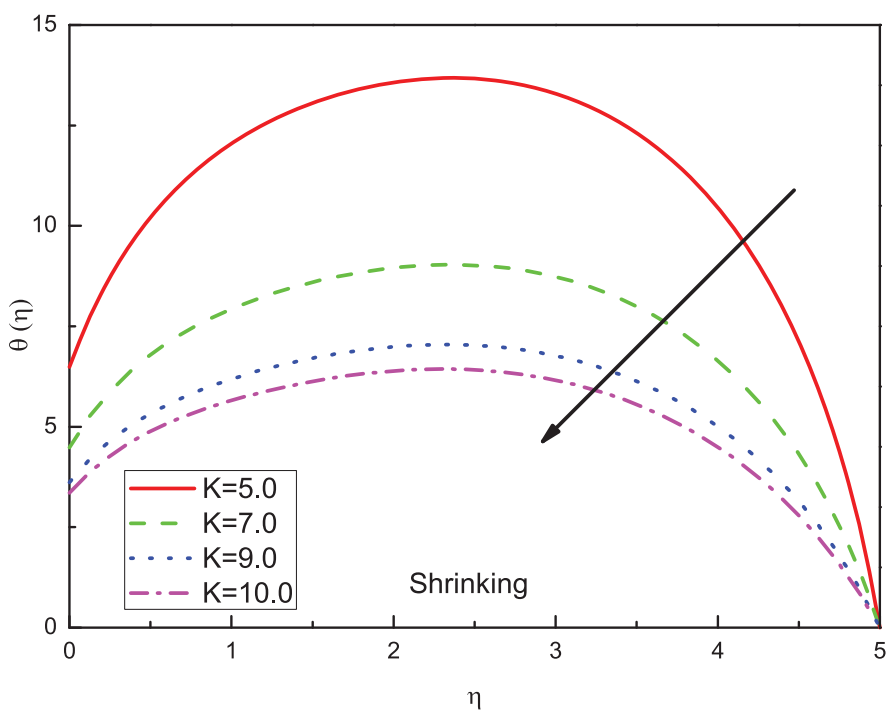


Figure 5. Variation of $\theta(\eta)$ vs. K in shrinking case.

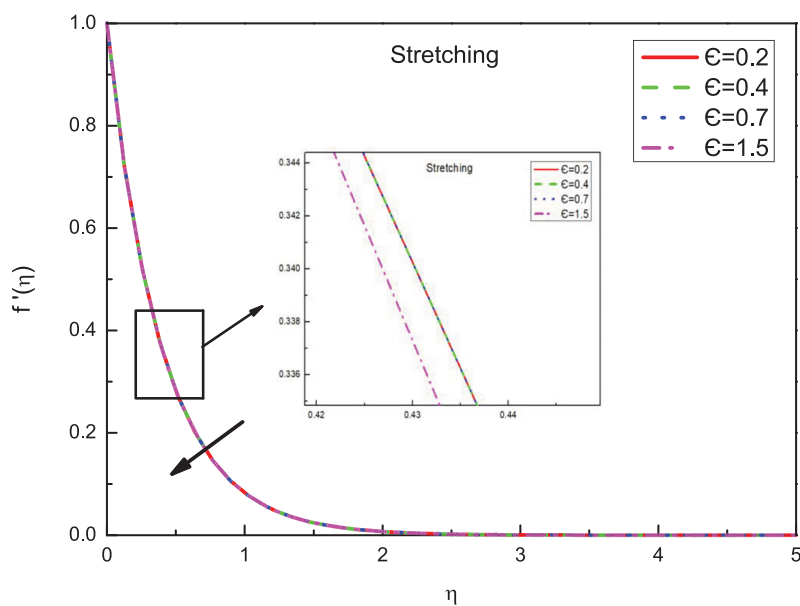


Figure 6. Variation of $f'(\eta)$ vs. ϵ in stretching case.

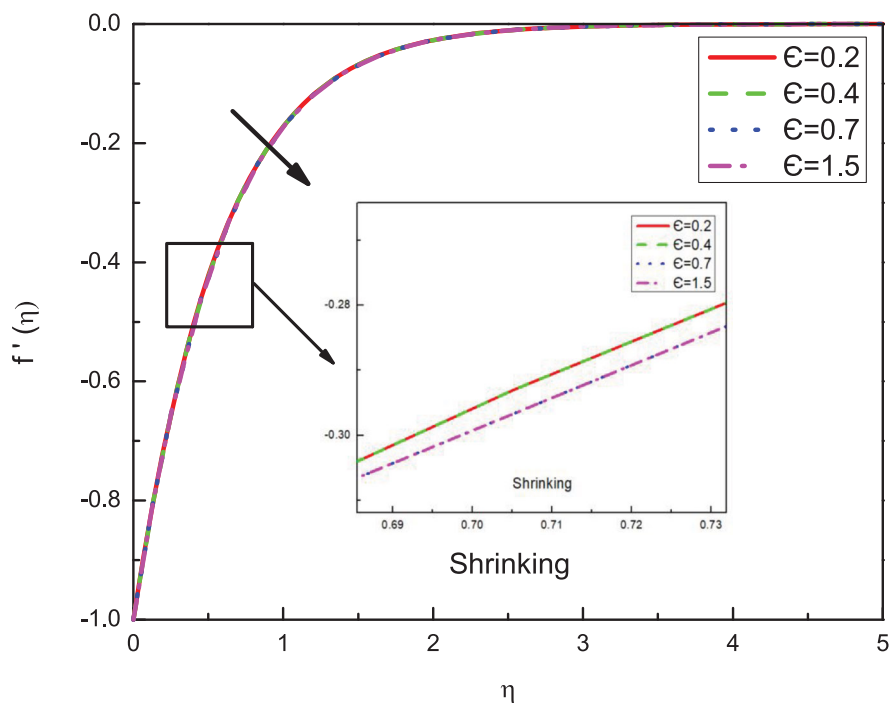


Figure 7. Variation of $f'(\eta)$ vs. ϵ in shrinking case.

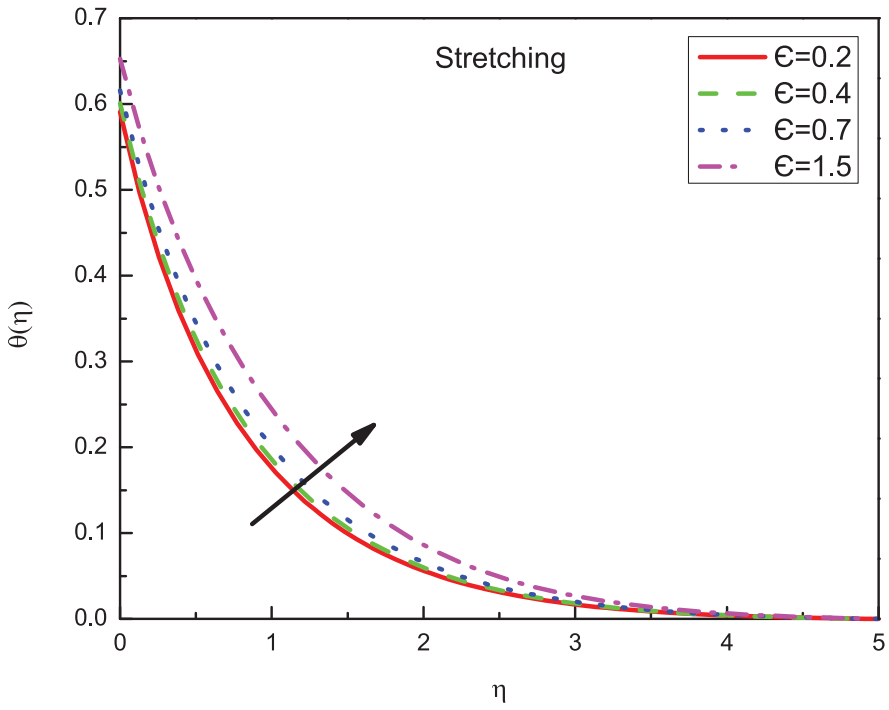


Figure 8. Variation of $\theta(\eta)$ vs. ϵ in stretching case.

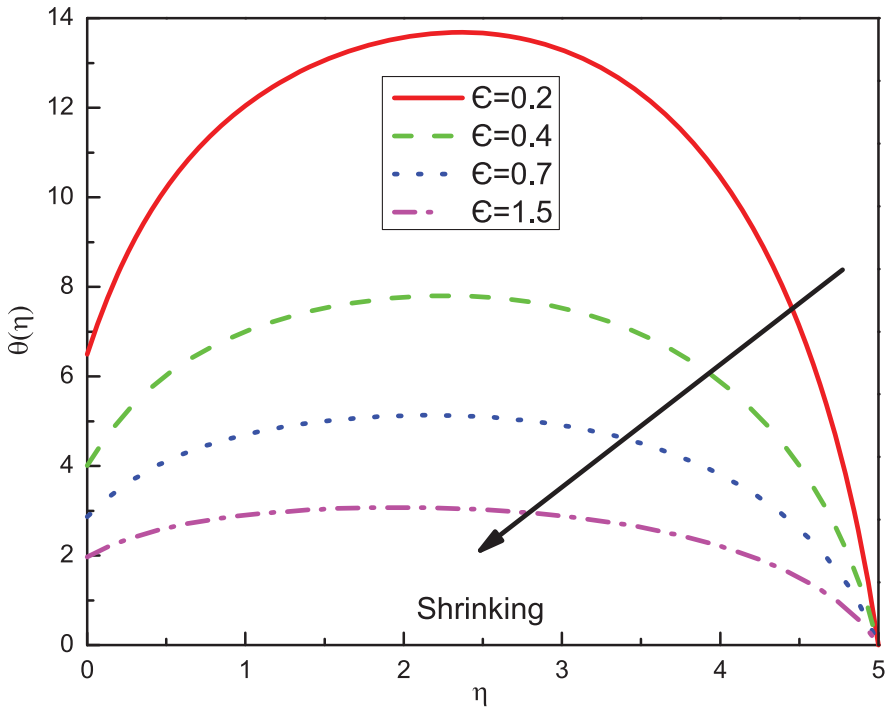


Figure 9. Variation of $\theta(\eta)$ vs. ϵ in shrinking case.

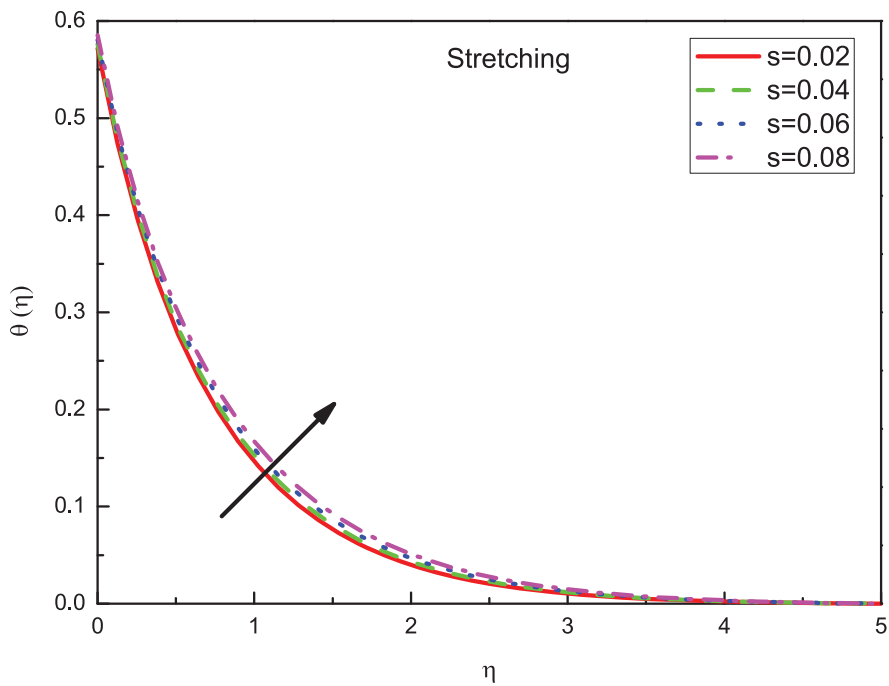


Figure 10. Variation of $\theta(\eta)$ vs. s in stretching case.

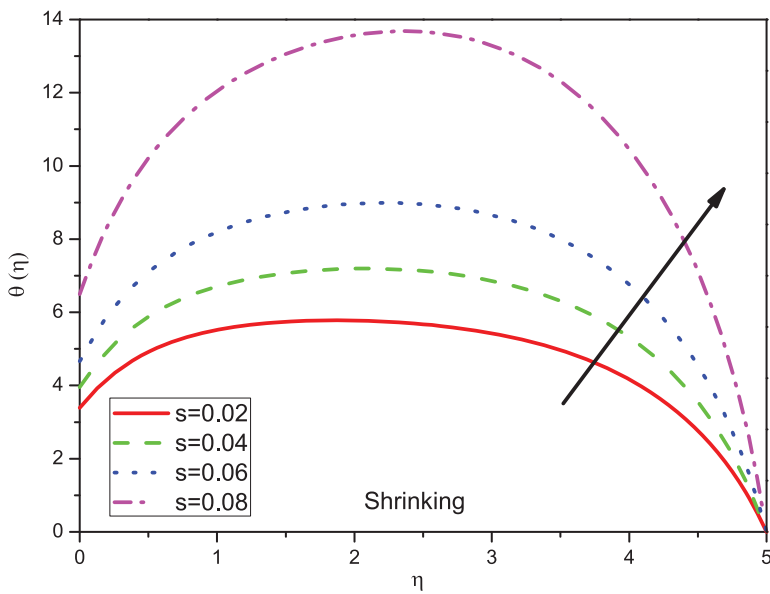


Figure 11. Variation of $\theta(\eta)$ vs. s in shrinking case.

velocity distribution in both cases stretching ($\lambda > 0$) and shrinking ($\lambda < 0$) for constant values of other parameters, and the momentum boundary layer thickness also is decreased in both states.

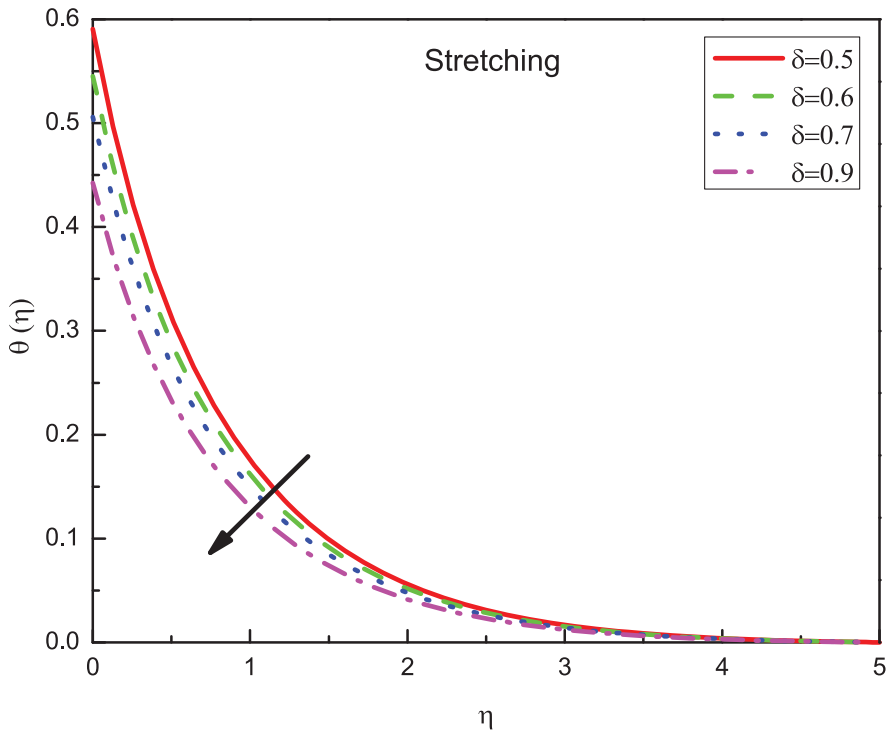


Figure 12. Variation of $\theta(\eta)$ vs. δ in stretching case.

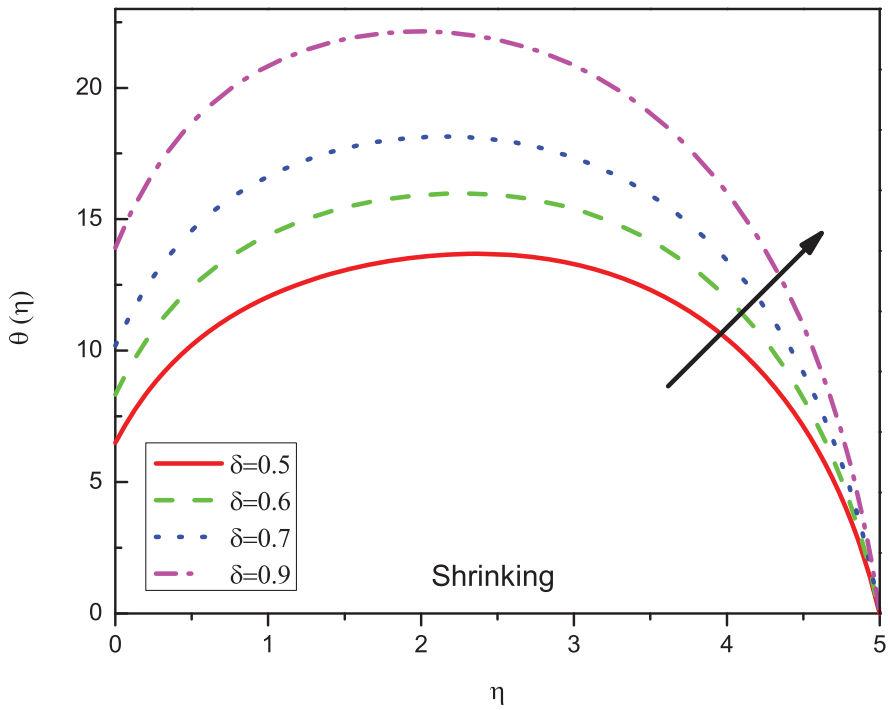


Figure 13. Variation of $\theta(\eta)$ vs. δ in shrinking case.

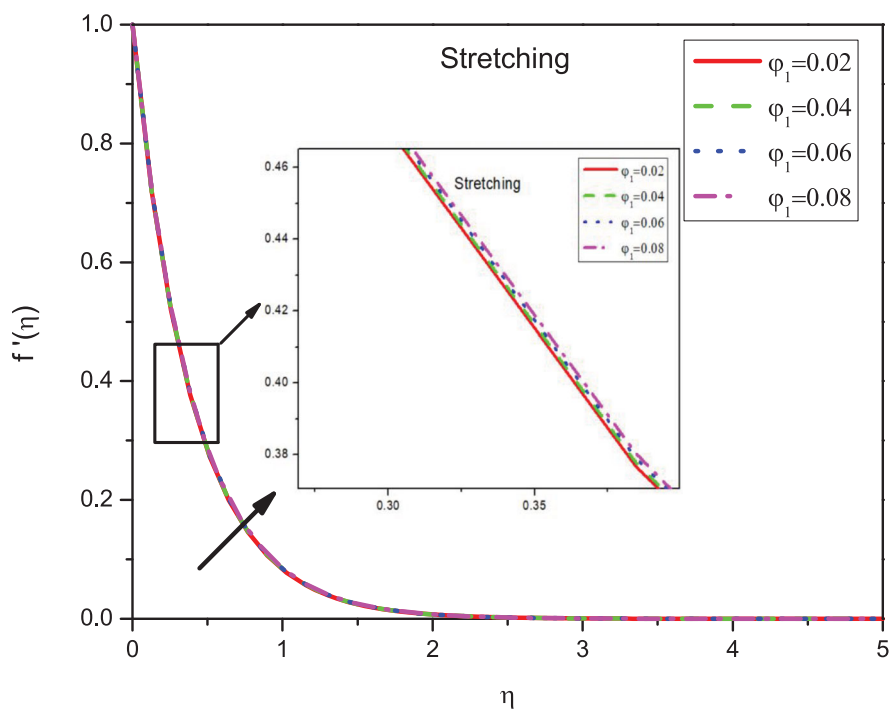


Figure 14. Variation of $f'(\eta)$ vs. φ_1 in stretching case.

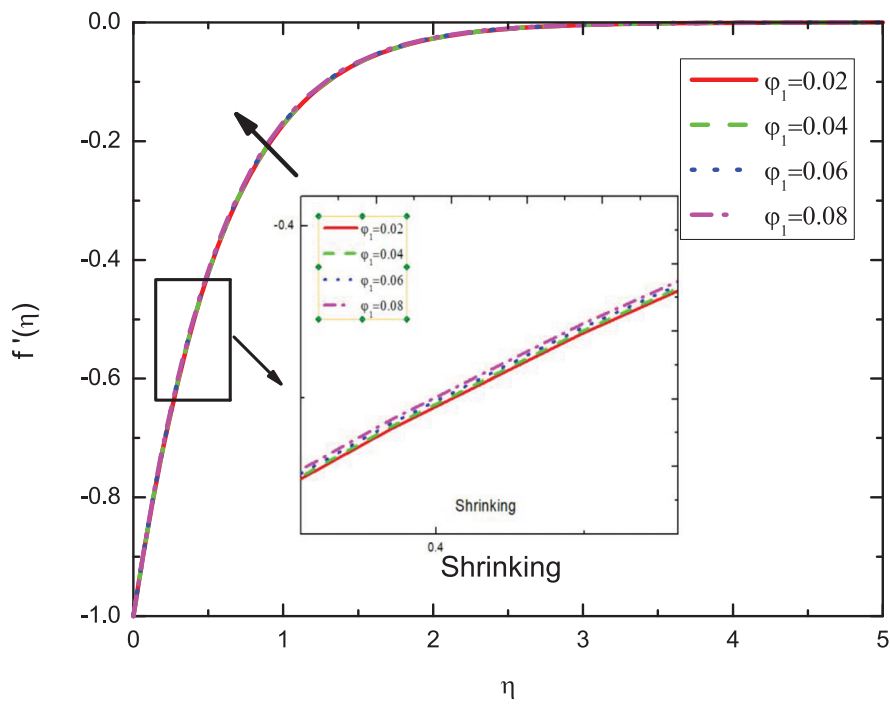


Figure 15. Variation of $f'(\eta)$ vs. φ_1 in shrinking case.

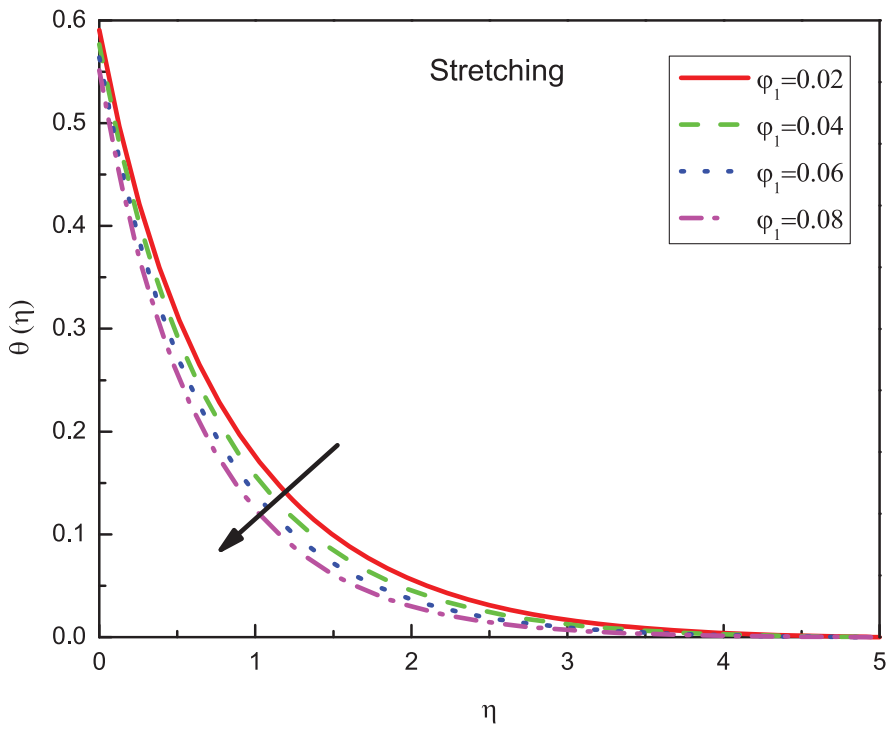


Figure 16. Variation of $\theta(\eta)$ vs. φ_1 in stretching case.

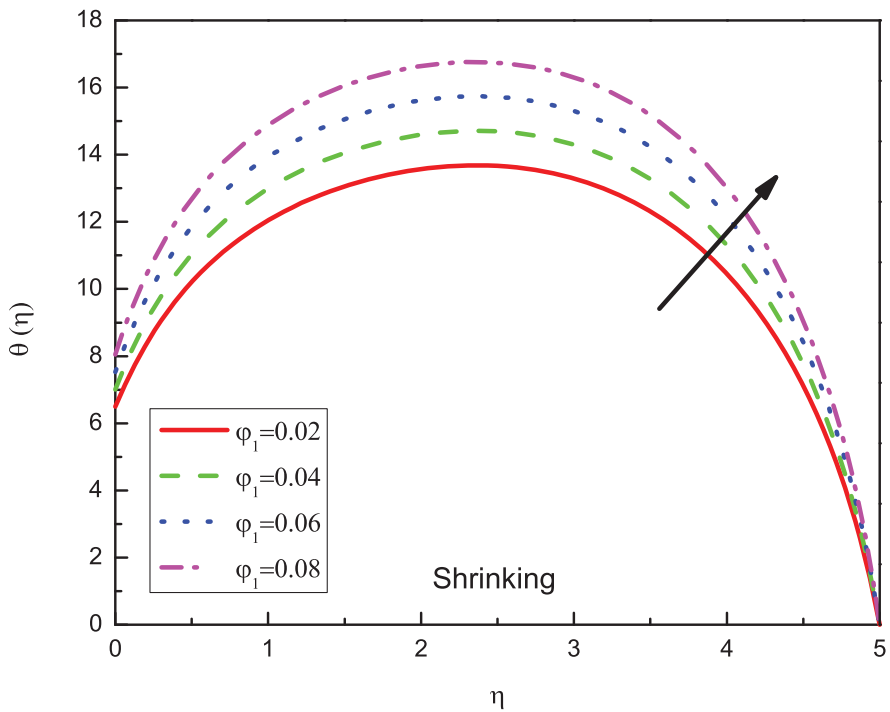


Figure 17. Variation of $\theta(\eta)$ vs. φ_1 in shrinking case.

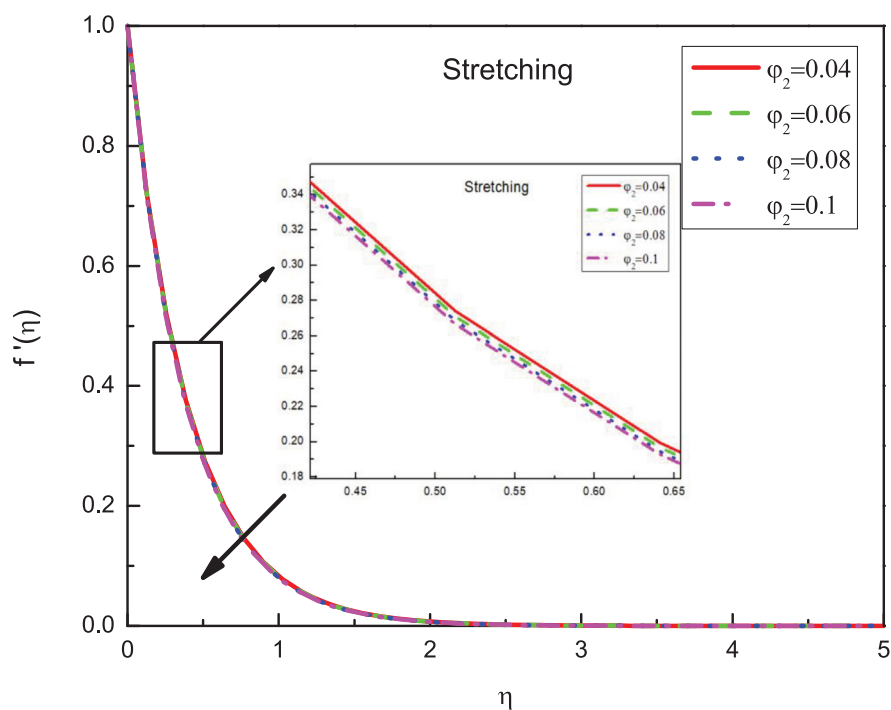


Figure 18. Variation of $f'(\eta)$ vs. φ_2 in stretching case.

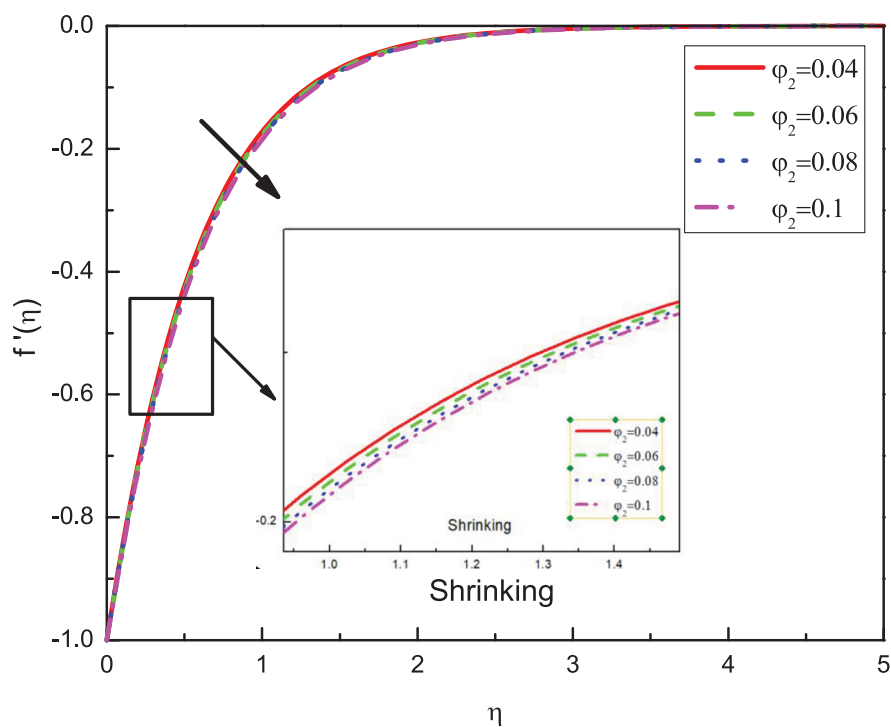


Figure 19. Variation of $f'(\eta)$ vs. φ_2 in shrinking case.

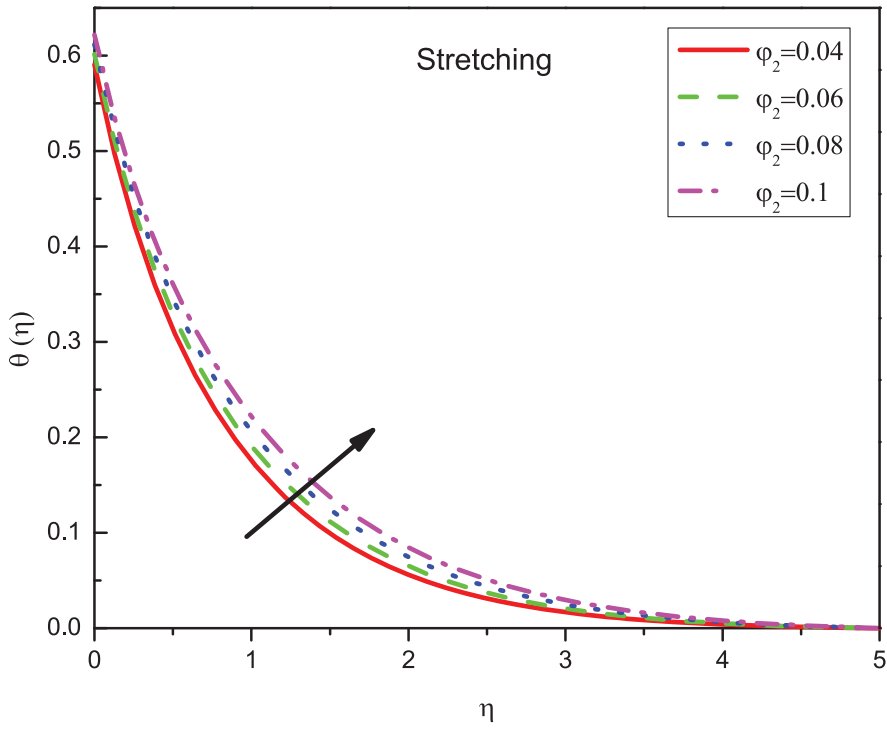


Figure 20. Variation of $\theta(\eta)$ vs. φ_2 in stretching case.

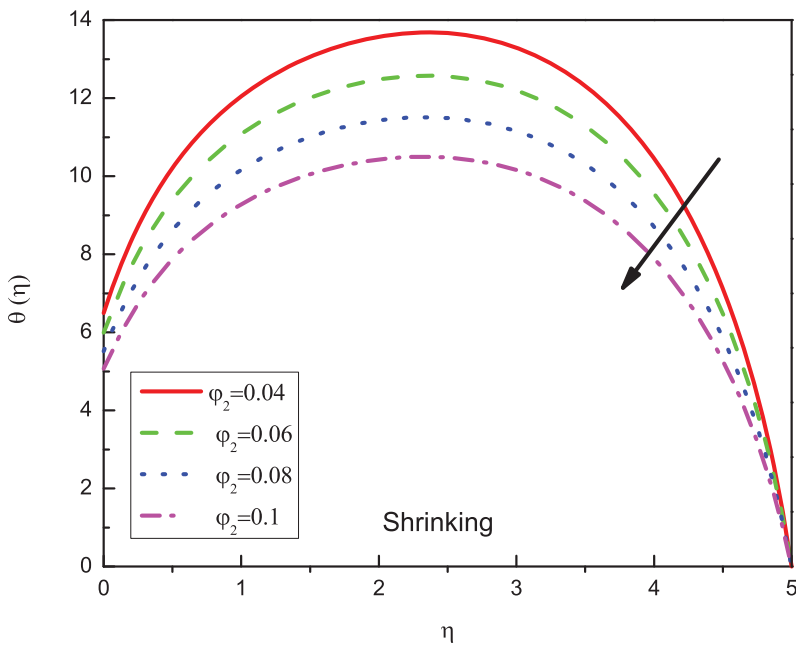


Figure 21. Variation of $\theta(\eta)$ vs. φ_2 in shrinking case.

Figures 8 and 9 show the influences of the parameter ϵ on the temperature graph. As the values of ϵ grow, the temperature value and the corresponding boundary-layer thickness is increased in the case ($\lambda > 0$). Where the temperature value and also, the thermal boundary-layer thickness is diminished in case ($\lambda < 0$) for fixed amounts of other parameters. Figures 10 and 11 represent the temperature graph $\theta(\eta)$ versus η , where the influences of heat generation/absorption parameter s on temperature when the other parameters are stationary. As the values of s increase, the temperature graph is enhanced in both cases stretching and shrinking, and as a result, the thermal boundary layer thickness rises. Physically, the thermal source can apply extra heat to the boundary-layer area and boosts the thermal boundary-layer thickness and diminishes the heat transfer rate from the surface to the fluid.

Figures 12 and 13 exhibit the impacts of slip parameter δ on temperature distribution for stretching and shrinking states when the other parameters are stationary. It is remarked that temperature distribution and the corresponding boundary-layer thickness are decreased with increasing δ in stretching state, due to the resistances of fluid movement at the surface decreases for the higher values of slip parameter as shown in Figure 12. However, the temperature distribution and the corresponding boundary-layer thickness are improved with growing δ in shrinking state as seen in Figure 13. Figures 14 and 15 illustrate the impact of solid volume fraction of Fe_3O_4 parameter φ_1 on velocity distribution $f'(\eta)$ for both cases ($\lambda > 0$) and ($\lambda < 0$), respectively, when the other parameters are fixed. It is noticed that the growing values of φ_1 increases the velocity and momentum boundary-layer thickness in both conditions ($\lambda > 0$) and ($\lambda < 0$), which may be that of greater collision between the suspended nanoparticles.

Figures 16 and 17 display the impact of solid volume fraction of Fe_3O_4 parameter φ_1 on temperature distribution $\theta(\eta)$ for both cases ($\lambda > 0$) and ($\lambda < 0$), respectively. When the other parameters are constant. It is noticed that the rising amounts of φ_1 diminish the temperature and the thermal boundary-layer thickness in stretching situation as seen in Figure 16. Including addition of nanoparticles can use more energy, which improves the temperature and subsequently thermal thickness in shrinking condition as demonstrated in Figure 17. Figures 18 and 19 exhibit the effects of solid volume fraction of Cu parameter φ_2 on velocity profiles for ($\lambda > 0$) and ($\lambda < 0$) for constant values of other parameters. It is observed that the velocity and the momentum boundary layer thickness are reduced with increasing φ_2 in both conditions ($\lambda > 0$) and ($\lambda < 0$). This is because of the collisions of suspended nanoparticles. Figures 20 and 21 depict the influences of parameter φ_2 on temperature distribution for stretching ($\lambda > 0$) and shrinking ($\lambda < 0$) cases for fixed values of other parameters. It is noticed that temperature and the thermal boundary layer thickness are increased with growing φ_2 in case ($\lambda > 0$). This behavior is consistent with the fact that solid particles have higher thermal conductivity than the thermal conductivity of the base fluid. But it is decreased in case ($\lambda < 0$) as seen in Figure 21. It is clear from Figures 22 and 23 that the Nusselt number ($Re_x^{-1/2}Nu_x$) is increased as parameter K and parameter ϵ increases in stretching case ($\lambda > 0$) and is reduced in shrinking case ($\lambda < 0$), respectively.

Figures 24 and 25 demonstrate the variations of skin fraction coefficient ($Re_x^{1/2}C_f$) against φ_1 for different values of φ_2 . The skin fraction coefficient ($Re_x^{1/2}C_f$) is increased with the raising in φ_1 and φ_2 parameters as viewed in Figure 24 in stretching case ($\lambda > 0$) and is diminished in shrinking case ($\lambda < 0$) as shown in Figure 25, for constant values of other parameters. The Nusselt number ($Re_x^{-1/2}Nu_x$) is reduced with the increasing of φ_1 and φ_2

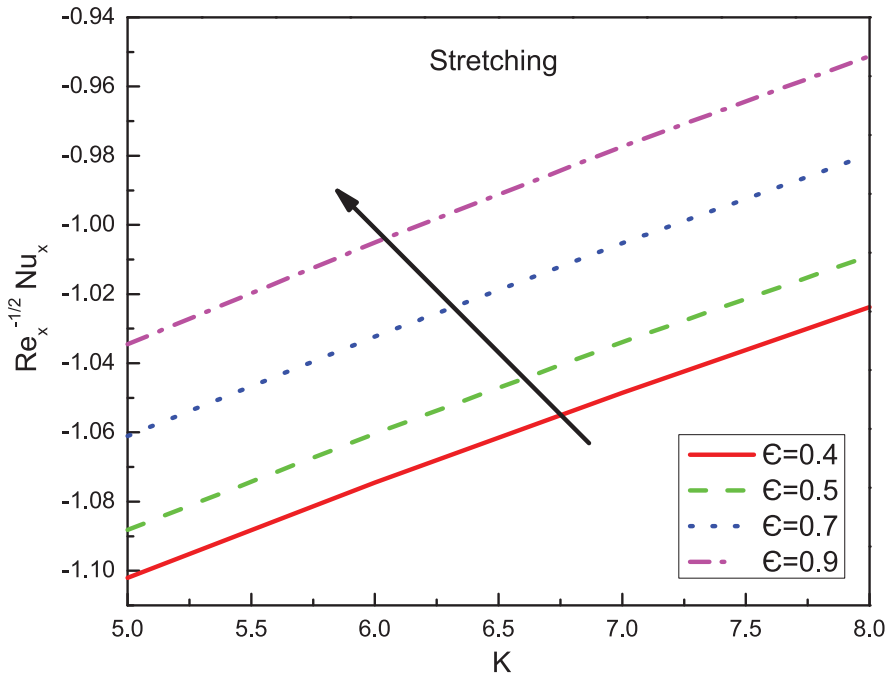


Figure 22. Variation of $Re_x^{-1/2} Nu_x$ vs. K with ϵ in stretching case.

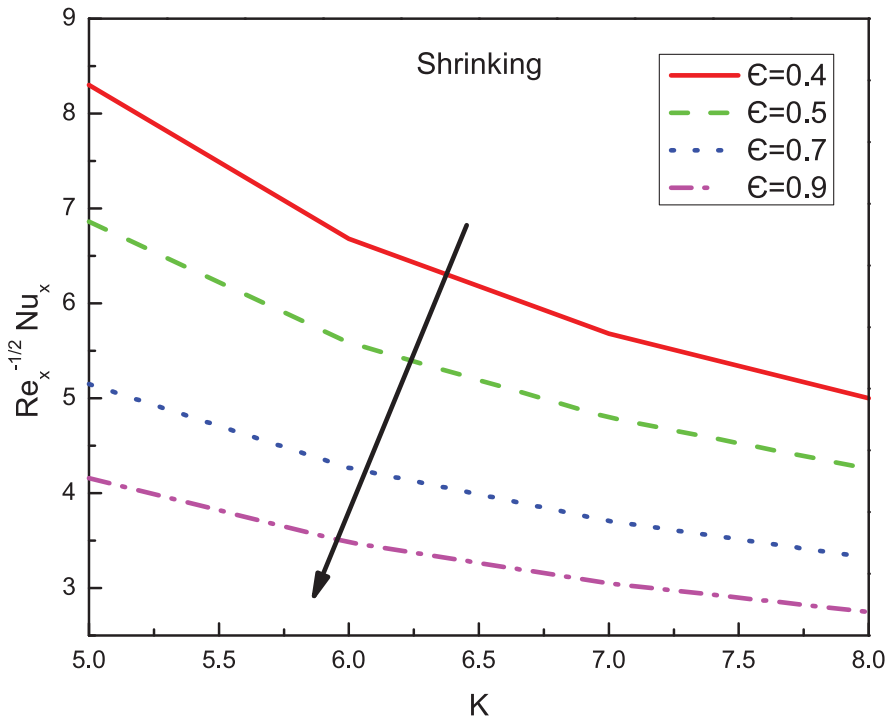


Figure 23. Variation of $Re_x^{-1/2} Nu_x$ vs. K with ϵ in shrinking case.

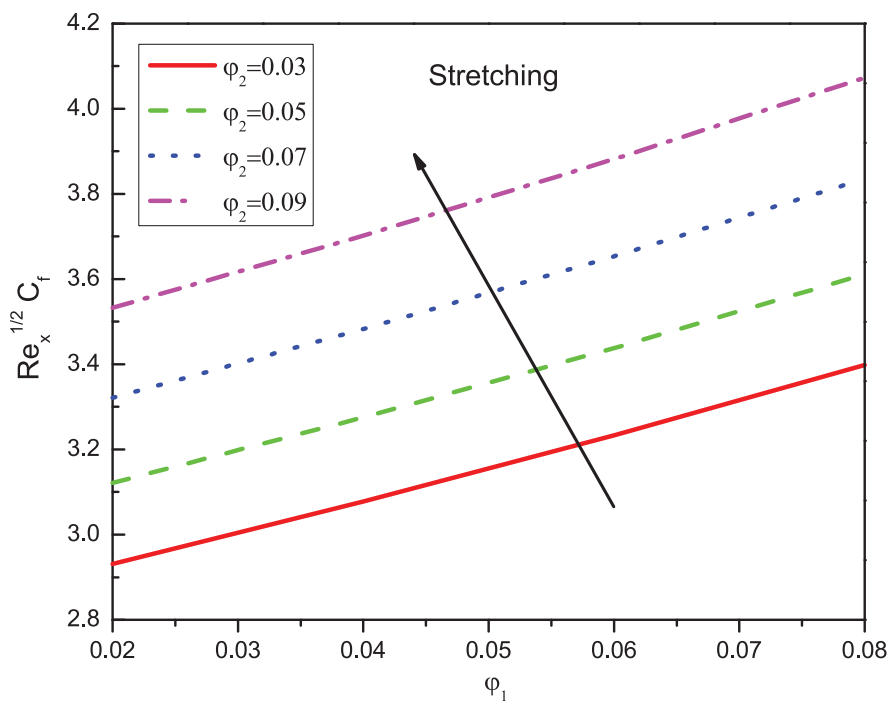


Figure 24. Variation of $Re_x^{1/2} C_f$ vs. ϕ_1 with ϕ_2 in stretching case.

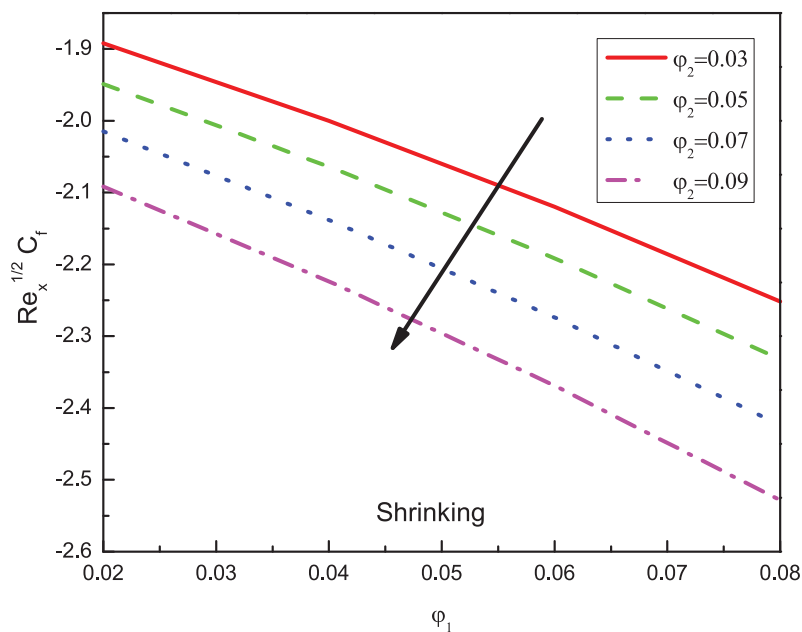


Figure 25. Variation of $Re_x^{1/2} C_f$ vs. ϕ_1 with ϕ_2 in shrinking case.

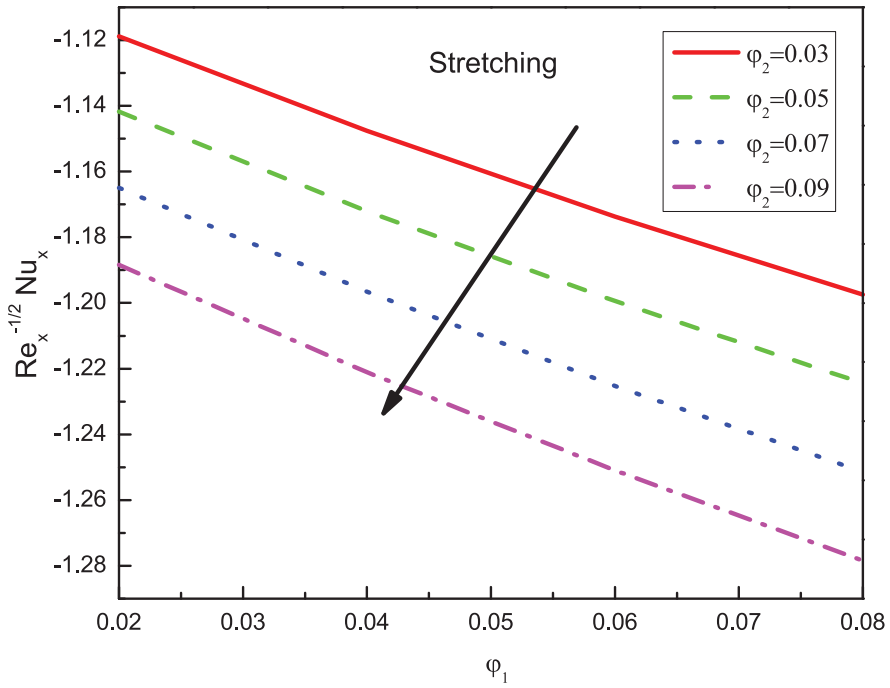


Figure 26. Variation of $Re_x^{-1/2} Nu_x$ vs. φ_1 with φ_2 in stretching case.

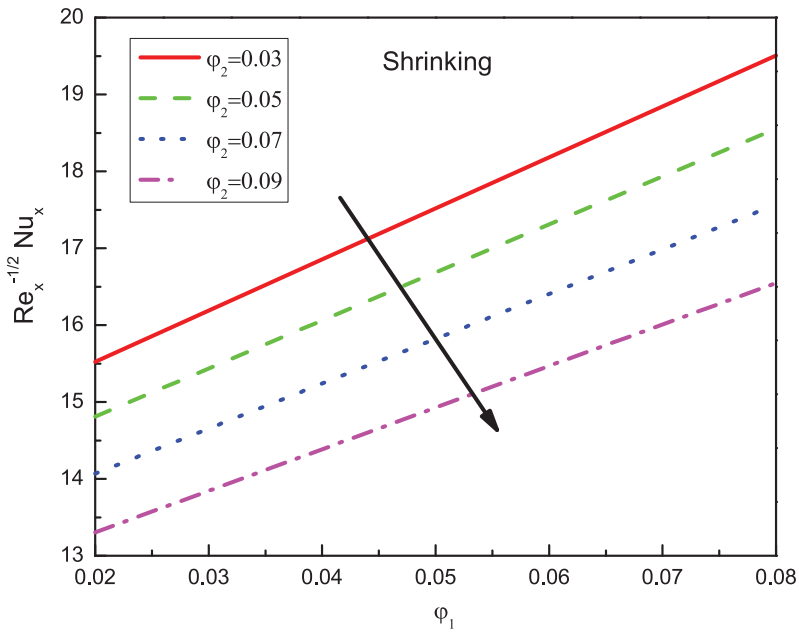


Figure 27. Variation of $Re_x^{-1/2} Nu_x$ vs. φ_1 with φ_2 in shrinking case.

parameters in the stretching ($\lambda > 0$) situation as displayed in Figure 26, but in shrinking ($\lambda < 0$) situation, the Nusselt number ($Re_x^{-1/2}Nu_x$) is boosted with the growing φ_1 and it is reduced with the increasing of φ_2 as offered in Figure 27, this is a result of the larger thermal conductivity of Cu nanoparticles.

5. Conclusions

This investigation aims to solve the steady laminar MHD hybrid nanofluid flow and heat transfer through an exponentially stretching or shrinking sheet in a porous material numerically. The slip condition and the heat source or sink are taken into consideration. The key observations are briefed as follows:

- The velocity profile is reduced with the increasing values of ϵ parameter for fixed values of other parameters.
- As the values of heat generation/absorption parameter s upsurge, the temperature is enhanced.
- The temperature is a decreasing function of δ in a stretching case while the opposite occurs in a shrinking situation.
- While the magnetite nanoparticles rise the flow velocity, the copper nanoparticles diminish the velocity in a stretching case. The opposite trend happens in a shrinking sheet situation.
- Nusselt number ($Re_x^{-1/2}Nu_x$) is reduced with the increasing of φ_1 and φ_2 in the case of a stretching sheet, while in the situation of a shrinking sheet it is boosted with an increment of φ_1 .
- Drag force ($Re_x^{1/2}C_f$) is raised with both nanoparticles in the case of stretching whilst the contrary happens in the shrinking case.

Disclosure statement

No potential conflict of interest was reported by the author(s).

ORCID

Mohamed R. Eid  <http://orcid.org/0000-0003-2479-9809>

References

- [1] Choi SUS. Enhancing thermal conductivity of fluids with nanoparticles. Proceedings of the 1995 ASME international mechanical engineering congress and exposition, FED 231/MD, New York, NY, USA; Vol. 66; 1995. p. 99–105.
- [2] Hwang KS, Lee JH, Jang SP. Buoyancy-driven heat transfer of water-based Al_2O_3 nanofluids in a rectangular cavity. *Int J Heat Mass Transfer*. 2007;50:4003–4010.
- [3] Buongiorno J. Convective transport in nanofluids. *ASME J Heat Transf*. 2006;128:240–250.
- [4] Tiwari RK, Das MK. Heat transfer augmentation in a two-sided lid-driven differentially heated square cavity utilizing nanofluids. *Int J Heat Mass Transfer*. 2007;50:2002–2018.
- [5] Kuznetsov AV, Nield DA. Natural convective boundary-layer flow of a nanofluid past a vertical plate. *Int J Therm Sci*. 2010;49:243–247.
- [6] Rohni AM, Ahmad S, Pop I. Boundary layer flow over a moving surface in a nanofluid beneath a uniform free stream. *Int J Heat Fluid Flow*. 2011;21:828–846.

- [7] Bachok N, Ishak A, Pop I. Flow and heat transfer over a rotating porous disk in a nanofluid. *Phys B Condens Matter*. 2011;406:1767–1772.
- [8] Rohni AM, Ahmad S, Pop I. Flow and heat transfer over an unsteady shrinking sheet with suction in nanofluids. *Int J Heat Mass Transf*. 2012;55:1888–1895.
- [9] Muhammad K, Hayat T, Alsaedi A, et al. Stagnation point flow of basefluid (gasoline oil), nano-material (CNTs) and hybrid nanomaterial (CNTs + CuO): a comparative study. *Mater Res Exp*. 2019;6(10):105003.
- [10] Reddy MGG, Kumar KG, Shehzad SA, et al. Thermal transportation analysis of nanoliquid squeezed flow past a sensor surface with MCWCNT and SWCNT. *Heat Transfer Asian Res*. 2019;48(6):2262–2275.
- [11] Muhammad K, Hayat T, Alsaedi A, et al. Numerical study of entropy production minimization in Bödewadt flow with carbon nanotubes. *Phys A Stat Mech Appl*. 2020;550:123966.
- [12] Muhammad K, Hayat T, Alsaedi A, et al. Melting heat transfer in squeezing flow of basefluid (water), nanofluid (CNTs + water) and hybrid nanofluid (CNTs + CuO + water). *J Therm Anal Calorim*. 2020:1–18. DOI:10.1007/s10973-020-09391-7.
- [13] Kumar KG, Avinash B, Rahimi-Gorji M, et al. Photocatalytic activity and smartness of TiO₂ nanotube arrays for room temperature acetone sensing. *J Mol Liq*. 2020;300:112418.
- [14] Suresh S, Venkitaraj KP, Selvakumar P, et al. Effect of Al₂O₃–Cu/water hybrid nanofluid in heat transfer. *Exp Thermal Fluid Sci*. 2012;38:54–60.
- [15] Baghbanzadeha M, Rashidib A, Rashtchiana D, et al. Synthesis of spherical silica/multi wall carbon nanotubes hybrid nano structures and investigation of thermal conductivity of related nanofluids. *Thermochim Acta*. 2012;549:87–94.
- [16] Nasrin R, Alim MA. Finite element simulation of forced convection in a flat plate solar collector: influence of nanofluid with double nanoparticles. *J Appl Fluid Mech*. 2014;7:543–556.
- [17] Takabi B, Shokouhmand H. Effects of Al₂O₃–Cu/water hybrid nanofluid on heat transfer and flow characteristics in turbulent regime. *Int J Mod Phys C*. 2015;26:1550047.
- [18] Devi SSU, Devi SPA. Numerical investigation of three-dimensional hybrid Cu–Al₂O₃/water nanofluid flow over a stretching sheet with effecting Lorentz force subject to Newtonian heating. *Can J Phys*. 2016;94:490–496.
- [19] Vafaei M, Afrand M, Sina N, et al. Evaluation of thermal conductivity of MgO–MWCNTs/EG hybrid nanofluids based on experimental data by selecting optimal artificial neural networks. *Phys E Low Dimens Syst Nanostruct*. 2017;85:90–96.
- [20] Devi SSU, Devi SPA. Heat transfer enhancement of Cu–Al₂O₃/water hybrid nanofluid flow over a stretching sheet. *J Nigerian Math Soc*. 2017;36:419–433.
- [21] Ibrahim F, Hady F, Abdel-Gaied S, et al. Influence of chemical reaction on heat and mass transfer of non-Newtonian fluid with yield stress by free convection from vertical surface in porous medium considering Soret effect. *Appl Math Mech*. 2010;31(6):675–684.
- [22] Hady F, Eid MR, Ahmed MA. Slip effects on unsteady MHD stagnation point flow of a nanofluid over stretching sheet in a porous medium with thermal radiation. *J Pure Appl Math Adv Appl*. 2014;12(2):181–206.
- [23] Hady F, Ibrahim F, Abdel-Gaied S, et al. Influence of yield stress on free convective boundary-layer flow of a non-Newtonian nanofluid past a vertical plate in a porous medium. *J Mech Sci Tech*. 2011;25(8):2043.
- [24] Hady F, Ibrahim F, Abdel-Gaied S, et al. Effect of heat generation/absorption on natural convective boundary-layer flow from a vertical cone embedded in a porous medium filled with a non-Newtonian nanofluid. *Int Commun Heat Mass Transfer*. 2011;38(10):1414–1420.
- [25] Hady F, Ibrahim F, Abdel-Gaied S, et al. Boundary-layer non-Newtonian flow over vertical plate in porous medium saturated with nanofluid. *Appl Math Mech*. 2011;32(12):1577–1586.
- [26] Eid MR. Chemical reaction effect on MHD boundary-layer flow of two-phase nanofluid model over an exponentially stretching sheet with a heat generation. *J Mol Liq*. 2016;220:718–725.
- [27] Eid MR. Time-dependent flow of water-NPs over a stretching sheet in a saturated porous medium in the stagnation-point region in the presence of chemical reaction. *J Nanofluids*. 2017;6(3):550–557.

- [28] Eid MR, Mahny KL. Unsteady MHD heat and mass transfer of a non-Newtonian nanofluid flow of a two-phase model over a permeable stretching wall with heat generation/absorption. *Adv Powder Technol.* **2017**;28(11):3063–3073.
- [29] Eid MR, Alsaedi A, Muhammad T, et al. Comprehensive analysis of heat transfer of gold-blood nanofluid (Sisko-model) with thermal radiation. *Results Phys.* **2017**;7:4388–4393.
- [30] Eid MR, Mahny KL. Flow and heat transfer in a porous medium saturated with a Sisko nanofluid over a non-linearly stretching sheet with heat generation/absorption. *Heat Transfer Asian Res.* **2018**;47:54–71.
- [31] Eid MR, Makinde OD. Solar radiation effect on a magneto nanofluid flow in a porous medium with chemically reactive species. *Int J Chem Reactor Eng.* **2018**;16(9):20170212.
- [32] Eid MR, Mahny K, Dar A, et al. Numerical study for Carreau nanofluid flow over a convectively heated nonlinear stretching surface with chemically reactive species. *Phys A Stat Mech Appl.* **2020**;540:123063.
- [33] Lahmar S, Kezzar M, Eid MR, et al. Heat transfer of squeezing unsteady nanofluid flow under the effects of an inclined magnetic field and variable thermal conductivity. *Phys A Stat Mech Appl.* **2020**;540:123138.
- [34] Eid MR. Effects of NP shapes on non-Newtonian bio-nanofluid flow in suction/blowing process with convective condition: Sisko model. *J Non Equilib Thermodyn.* **2020**;45(2):97–108.
- [35] Eid MR, Mabood F. Entropy analysis of a hydromagnetic micropolar dusty carbon NTs-kerosene nanofluid with heat generation: Darcy–forchheimer scheme. *J Therm Anal Calorim.* **2020**. DOI:10.1007/s10973-020-09928-w.
- [36] Qayyum S, Khan MI, Hayat T, et al. A framework for nonlinear thermal radiation and homogeneous-heterogeneous reactions flow based on silver-water and copper-water nanoparticles: a numerical model for probable error. *Results Phys.* **2017**;7:1907–1914.
- [37] Hayat T, Khan MI, Waqas M, et al. Numerical simulation for melting heat transfer and radiation effects in stagnation point flow of carbon–water nanofluid. *Comput Methods Appl Mech Eng.* **2017**;315:1011–1024.
- [38] Aparna Z, Michael M, Pabi SK, et al. Thermal conductivity of aqueous $\text{Al}_2\text{O}_3/\text{Ag}$ hybrid nanofluid at different temperatures and volume concentrations: an experimental investigation and development of new correlation function. *Powder Tech.* **2019**;343:714–722.
- [39] Gulzar O, Qayoum A, Gupta R. Experimental study on stability and rheological behaviour of hybrid $\text{Al}_2\text{O}_3\text{-TiO}_2$ Therminol-55 nanofluids for concentrating solar collectors. *Powder Tech.* **2019**;352:436–444.
- [40] Magyari E, Keller B. Heat and mass transfer in the boundary layers on an exponentially stretching continuous surface. *J Phys D Appl Phys.* **1999**;32:577–585.
- [41] El-Aziz MA. Viscous dissipation effect on mixed convection flow of a micropolar fluid over an exponentially stretching sheet. *Can J Phys.* **2009**;87:359–368.
- [42] Sajid M, Hayat T. Influence of thermal radiation on the boundary layer flow due to an exponentially stretching sheet. *Int Commun Heat Mass Transf.* **2008**;35:347–356.
- [43] Bidin B, Nazar R. Numerical solution of the boundary layer flow over an exponentially stretching sheet with thermal radiation. *Eur J Sci Res.* **2009**;33:710–717.
- [44] Souayah B, Kumar KG, Reddy MG, et al. Slip flow and radiative heat transfer behavior of Titanium alloy and ferromagnetic nanoparticles along with suspension of dusty fluid. *J Mol Liq.* **2019**;290:111223.
- [45] Kumar KG, Reddy MG, Shehzad S, et al. A least square study on flow and radiative heat transfer of a hybrid nanofluid in a moving frame by considering a spherically-shaped particle. *Rev Mex Fis.* **2020**;66(2):162–170.
- [46] Bhattacharyya K, Pop I. MHD boundary layer flow due to an exponentially shrinking sheet. *Magnetohydrodyn.* **2011**;47:337–344.
- [47] Nadeem S, Ul Haq R, Lee C. MHD flow of a Casson fluid over an exponentially shrinking sheet. *Sci Iran.* **2012**;19:1550–1553.
- [48] Ishak A. MHD boundary layer flow due to an exponentially stretching sheet with radiation effect. *Sains Malays.* **2011**;40:391–395.

- [49] Mabood F, Khan WA, Ismail AIM. MHD flow over exponential radiating stretching sheet using homotopy analysis method. *J King Saud Univ Eng Sci.* [2017](#);29:68–74.
- [50] Waini I, Ishak A, Pop I. Hybrid nanofluid flow induced by an exponentially shrinking sheet. *Chin J Phys.* [2019](#). DOI:[10.1016/j.cjph.2019.12.015](#).
- [51] Dinarvand S. Nodal/saddle stagnation-point boundary layer flow of CuO–Ag/water hybrid nanofluid: a novel hybridity model. *Microsyst Technol.* [2019](#);25:2609–2623.
- [52] Hady FM, Ibrahim FS, Abdel-Gaied SM, et al. Radiation effect on viscous flow of a nanofluid and heat transfer over a nonlinearly stretching sheet. *Nanoscale Res Lett.* [2012](#);7(1):229.